

# Molecular Dynamics Simulations of Orientation Effects During Tension, Compression, and Bending Deformations of Magnesium Nanocrystals

Haidong Fan<sup>1</sup>

Department of Mechanical Engineering,  
Johns Hopkins University,  
Baltimore, MD 21218;  
Department of Mechanics,  
Sichuan University,  
Chengdu, Sichuan 610065, China  
e-mail: haidongfan8@foxmail.com

Jaafar A. El-Awady

Department of Mechanical Engineering,  
Johns Hopkins University,  
Baltimore, MD 21218  
e-mail: jelawady@jhu.edu

The deformation modes in magnesium nanocrystals during uniaxial tension, uniaxial compression, and pure bending are investigated using molecular dynamics (MD) simulations at room temperature. For each loading condition, the crystal orientation effects are studied by increasing the crystal *c*-axis orientation angle  $\theta$  relative to the loading direction from 0 deg to 90 deg by a 15 deg increment. The simulation results reveal a number of different deformation modes and an obvious tension-compression asymmetry in magnesium nanocrystals. As the *c*-axis is rotated away from the tension loading direction, the deformation mode at yielding changes from tension twinning ( $\theta \leq 45$  deg) to compression twinning ( $\theta > 45$  deg). For compression loading, yielding is dominated by only dislocation slip on the pyramidal ( $\theta < 15$  deg), basal ( $15 \text{ deg} < \theta < 60$  deg) and prismatic ( $\theta > 60$  deg) planes. The nucleation stress in general decreases with increasing  $\theta$  for both uniaxial tension and uniaxial compression loadings. For pure bending simulations, the yielding is mostly controlled by the weaker deformation mode between the compressive and tensile sides. The bending nucleation stress also decreases as the *c*-axis deviates away from the loading direction. [DOI: 10.1115/1.4030930]

**Keywords:** molecular dynamics, magnesium, bending, Nanocrystals, orientation

## 1 Introduction

Magnesium (Mg) and its alloys demonstrate excellent properties, including high specific strength, superior damping capacity, high thermal conductivity, and efficient recyclability, which make them an attractive structural material for automotive, aerospace, electronic, and defense applications. However, a widespread commercial utilization of these materials is still challenging because of some critical limitations, including poor ductility, poor formability at ambient temperature, and degradation of mechanical properties at elevated temperatures. The poor ductility originates from the anisotropy of the Mg hexagonal closed packed (HCP) crystalline structure, which cannot provide five independent easy slip systems as suggested by the von Mises criterion [1]. While there are ongoing experimental efforts to improve Mg ductility through alloying, grain refinement, and texture weakening, the underlying deformation mechanisms in Mg are still not well characterized. Therefore, it is vital to develop a systematic understanding of the fundamental deformation modes in Mg crystals.

In Mg, various deformation modes are potentially active under different loading conditions, including dislocation slip and twinning [2]. As summarized in Fig. 1, dislocation slip can occur on the basal (Ba), prismatic (Pr), first-order pyramidal (Py-I), and second-order pyramidal (Py-II) planes. Furthermore, two twinning modes can be characterized by the type of straining imposed along the *c*-axis. In the case of extension along the *c*-axis, extension

twins (or sometimes referred to as tension twins (TTs)) may occur on the {10–12} (TT<sub>1</sub>) and {11–21} (TT<sub>2</sub>) planes. On the other hand, in the case of contraction along the *c*-axis, contraction twins (or sometimes referred to as compression twins (CTs)) can occur along the {10–11} (CT<sub>1</sub>) and {11–22} (CT<sub>2</sub>) planes.

Micro- and nanopillar experiments were previously utilized to characterize the formation and evolution of possible deformation modes in Mg single crystals. In those experiments, only one or two predominant deformation modes were active for a specific loading orientation. During *c*-axis compression of pure Mg [3–6] and AZ31 [7] micropillars, pyramidal slip was typically observed during the early stage of deformation and strong strain hardening was also reported. Due to slight misalignment or misorientation, the deformation was subsequently dominated by massive basal slip bursts. In contrast, during *c*-axis compression of nanosized Mg pillars (diameter = 150 nm), compression twinning was observed instead of pyramidal slip, followed by extensive basal slip within the twin leading to strain softening [8]. On the other hand, in *c*-axis tension studies, tension twinning accompanied by strong strain hardening was observed [8]. Moreover, when the crystal *c*-axis deviates from the loading direction by  $45 \pm 25$  deg, basal slip is predominant since its Schmid factor is the largest [4,6,7,9,10]. Ultimately, during compression perpendicular to the *c*-axis, tension twinning prevails [4,10].

While the aforementioned experiments focused on the uniaxial response during compression or tension loading, the mechanical behavior during bending deformation has been rarely studied. Under bending loading, the material is exposed to both compression and tension states on opposite sides of the crystal, which would be expected to lead to multiple deformation modes

<sup>1</sup>Corresponding author.

Contributed by the Applied Mechanics Division of ASME for publication in the JOURNAL OF APPLIED MECHANICS. Manuscript received May 30, 2015; final manuscript received June 25, 2015; published online July 14, 2015. Assoc. Editor: Harold S. Park.

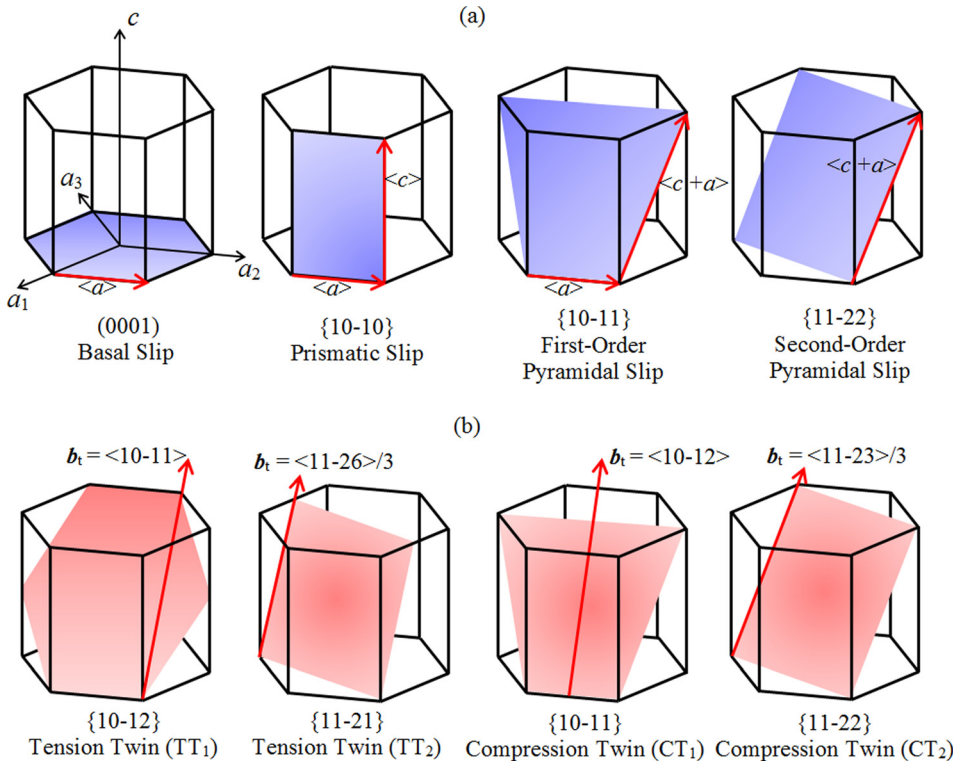


**Fig. 1 Schematic of the HCP unit cell showing all possible: (a) slip and (b) twinning systems. The planes are highlighted, and the Burgers vectors are shown by the red arrows (see online version for color).**

mutually. In a recent nanobending experimental study, Ye et al. [9] showed the development of both cracks and CTs on the tension and compression sides of the crystal, respectively.

A number of MD simulations were also performed as an effective tool to study the deformation modes in single-crystalline nanocrystals. Simulations of  $c$ -axis compression at room temperature predict a predominant deformation through compression twinning for nanopillars having sizes below 10 nm [11], while first-order pyramidal slip was observed in larger sizes at low temperature [12,13]. On the other hand, tension along  $c$ -axis was reported to lead to tension twinning [9,11], while basal slip prevails in nanocrystals loaded 45 deg away from the  $c$ -axis [11].

Discrete dislocation dynamics (DDD) simulations were also employed to study both dislocation-mediated plasticity and dislocation-twin boundary (TB) interactions in single and polycrystalline Mg [7,14–17]. From single-crystal DDD simulations, the massive basal slip observed experimentally during  $c$ -axis compression was confirmed to be a result of crystal misorientation [7]. In addition, dislocation-TB interactions were reported to be significant for the strain hardening and grain size-effects [14,17].

Although extensive experimental and simulation studies were conducted on the deformation modes of Mg, substantial discrepancy in the results still exists. In particular, in experimental observations,  $c$ -axis compression was usually reported to be mediated by second-order pyramidal slip [18,19]. In contrast, MD simulations suggested that first-order pyramidal slip is predominant [12,20,21]. More recent slip trace analysis of  $c$ -axis deformed experiments seems to support these simulation predictions [22]. Moreover, in both experiments and simulations, only three orientations are typically investigated, and a complete understanding of the orientation effects on the deformation modes is still missing. Therefore, here, the uniaxial tension, uniaxial compression, and pure bending deformations of single-crystal Mg nanocrystals having different orientations are investigated using MD simulations. In each loading condition, the crystal orientation effects are studied by progressively rotating the  $c$ -axis from 0 deg to 90 deg away from the loading direction.

This paper is organized as follows. The computational methods are discussed in Sec. 2, and the simulation results are presented and discussed in Sec. 3. Finally, concluding remarks are made in Sec. 4.

## 2 Computational Methods

In all the current simulations, a simulation cell mimicking a rectangular nanocrystal with edge-lengths  $l_x = 30$  nm,  $l_y = 30$  nm, and  $l_z = 60$  nm is considered. The total number of atoms in the simulation cell is  $\sim 2.38 \times 10^6$ . A two-dimensional schematic of the simulation cell cross section is shown in Fig. 2. Free surface boundary conditions are employed along all three directions. The crystal  $c$ -axis is oriented by an angle  $\theta$  away from the loading direction. Three-different loadings are employed, namely, uniaxial tension, uniaxial compression, and pure bending. For the tension and compression simulations, a uniform strain is imposed on the top and bottom surfaces with a total strain rate of  $\dot{\varepsilon} = 2 \times 10^8$  s $^{-1}$ . In the bending simulations, a bending moment is imposed on the top and bottom surfaces, as shown schematically in Fig. 2. The bending loading rate is  $\dot{M} = 26.67$  N·nm/s. To study the crystal orientation effects for each loading condition, the orientation angle  $\theta$  is varied from 0 deg to 90 deg by a 15 deg increment.

All simulations were performed using the three-dimensional MD simulator LAMMPS [23]. Two embedded atom method potentials developed by Sun et al. [24] and Liu et al. [25] are used to model the interatomic interaction. These two potentials were previously used extensively to study the deformation of Mg. As summarized in Ref. [12], the potentials agree well with the density functional theory and experimental measurements, in terms of lattice constants, cohesive energy, elastic constants, and stacking fault energies. In the following, unless otherwise noted, the simulation results reported are using the Liu et al.’s potential. At the beginning of all simulations, the atomic system is relaxed fully by the conjugate gradient algorithm. Then, the system is heated to 300 K within 50 ps, and the temperature is maintained constant during loading using the NVT ensemble. The time step is set to be

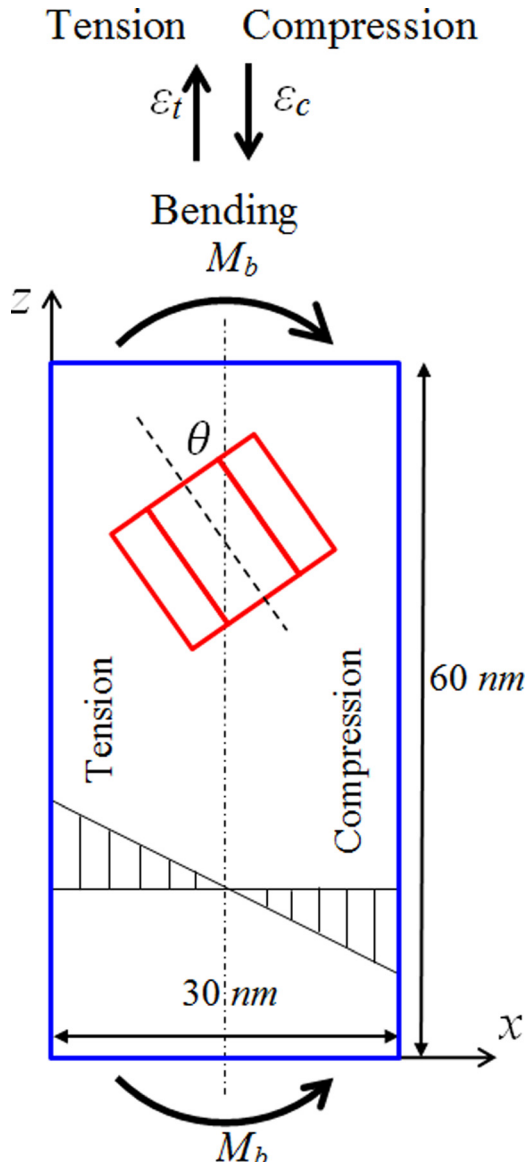


**Fig. 2** Cross section schematic of the  $30\text{ nm} \times 30\text{ nm} \times 60\text{ nm}$  simulation cell for the pure bending, uniaxial tension, and uniaxial compression simulations

0.001 ps. Since thermal fluctuation at room temperature leads to difficulties in clearly identifying the dislocation and twin structures, in most of the figures of this work, the fluctuations are removed by performing 50 steps of conjugate gradient relaxation. All atom visualizations are obtained using OVITO [26], while the centrosymmetry and common neighbor analysis (CNA) parameters are used to color the atoms, as indicated in each figure caption. The centrosymmetry parameter for HCP crystals is: 0 for stack faults or the FCC lattice; 9 for dislocation cores and TBs; 10 for HCP bulk lattice; and  $>12$  for free surfaces.

### 3 Results and Discussion

**3.1 Uniaxial Tension Deformation.** In this subsection, the tension deformation of Mg nanocrystals is reported. First, the simulation results for the  $\theta = 0\text{ deg}$  case are shown in Fig. 3. Two TTs with boundaries on the  $\{10\bar{1}2\}$  planes (i.e.,  $\text{TT}_1$ ) nucleate from the edges of the simulation cell, with the larger twin nucleating earlier from one of the simulation cell corners. The nucleation of these TTs agrees well with experimental observations [4,8]. In both the matrix and the twin, no dislocations are observed.

Furthermore, two types of interfaces between the matrix and the twin can be identified, including a horizontal basal/prismatic (B/P) transformation interface, and inclined TBs, as shown in Fig. 3(b), indicating good agreement with the experimental TEM observations [27]. Multiple parallel and stable stacking faults also reside on basal planes in the twinned region. Figure 3(c) shows the stacking sequence in the vicinity of one of these stacking faults. While these stacking faults are on basal planes, they are intrinsic faults with only one-atom-layer fault, which are different from the two-atom-layer faults formed by basal dislocations. As shown in Fig. 3(d), these faults always nucleate from the TBs or B/P interfaces and not from the free surfaces. Such stacking faults are probably significant for the TB migration and twin growth, which is beyond the focus of the current study.

Figure 4 shows the tensile deformation of the  $\theta = 15\text{ deg}$  case. In Fig. 4(a), a predominant twin nucleates near the loading end and pierces the simulation cell quickly in the absence of any dislocations or stacking faults in either the twin or the matrix. The orientations of the twin and the matrix indicate that the twin is a tension twin with boundaries on  $\{11\bar{2}1\}$  planes (i.e.,  $\text{TT}_2$ ). The same deformation mode is also predicted using the Sun et al.'s potential. This twin system has been previously reported in MD simulations with periodic boundary conditions of perfect crystals (i.e., homogenous nucleation) [28], or with an initial nanovoid or nanocrack [29]. It should be noted that the tensile deformation of Mg single crystals having this orientation has not been reported yet, and this twinning system has not been observed experimentally in pure Mg. Thus, the current predictions remain to be validated from pure Mg tensile experiments. Nevertheless, this twinning system was reported in Mg alloy ( $\text{Mg-5\%Y-2\%Nd-2\%RE-0.5\%Zr}$ ) in solution treated condition [30].

The tension simulation of a  $\theta = 30\text{ deg}$  case is shown in Fig. 5. In Fig. 5(a), both basal  $\langle a \rangle$  dislocations and  $\{11\bar{2}1\}$  twins are observed to nucleate near the loading ends and subsequently interact. Figures 5(b)-5(d) show a sequence of basal  $\langle a \rangle$  dislocation interactions with the  $\{11\bar{2}1\}$  twin. First, a basal dislocation nucleates from the bottom end and then glides toward the twin, as shown in Fig. 5(b). Subsequently, the dislocation intersects the first TB and transmits into the twin as a basal dislocation, as shown in Fig. 5(c). In Fig. 5(d), after intersecting the second TB, it finally glides back on the basal plane in the matrix. This sequence of interactions agrees well with the geometry based predictions of Yoo [31]

$$(0001)_M[\bar{1}\bar{1}20]/3 \rightarrow (0001)_T[\bar{1}\bar{1}20]/3 - 2b_t \quad (1)$$

or

$$(0001)_M[2\bar{1}10]/3 \rightarrow (0001)_T[\bar{2}110]/3 - b_t \quad (2)$$

Thus, basal dislocation intersections with this TB would lead to the formation of twinning dislocations with Burgers vector  $b_t$  on the TB, providing a possible mechanism for TB migration.

The tension simulation results of a  $\theta = 45\text{ deg}$  case are shown in Fig. 6. Similar to the  $\theta = 30\text{ deg}$  case, both basal dislocations and  $\{11\bar{2}1\}$  twinning are observed, as shown in Fig. 6(a). Two types of dislocation nucleation events can be identified: dislocations nucleating near the loading ends; and dislocations nucleating at the intersection between the TBs and the free surface (see Fig. 6(b)).

During tension simulations of the  $\theta = 60\text{ deg}$ ,  $75\text{ deg}$ , and  $90\text{ deg}$  cases,  $\{10\bar{1}1\}$  CTs are observed to dominate, with no dislocation activity observed, as shown in Fig. 7. Furthermore, many intrinsic stacking faults are observed within the twins.

Since the nanocrystals are initially defect-free, the mechanical response is generally controlled by the nucleation of defects from the free surfaces. The nucleation stress and corresponding first nucleating defect type (i.e., dislocation or twin) are summarized in Fig. 8 as a function of the simulation cell orientation angle. It is

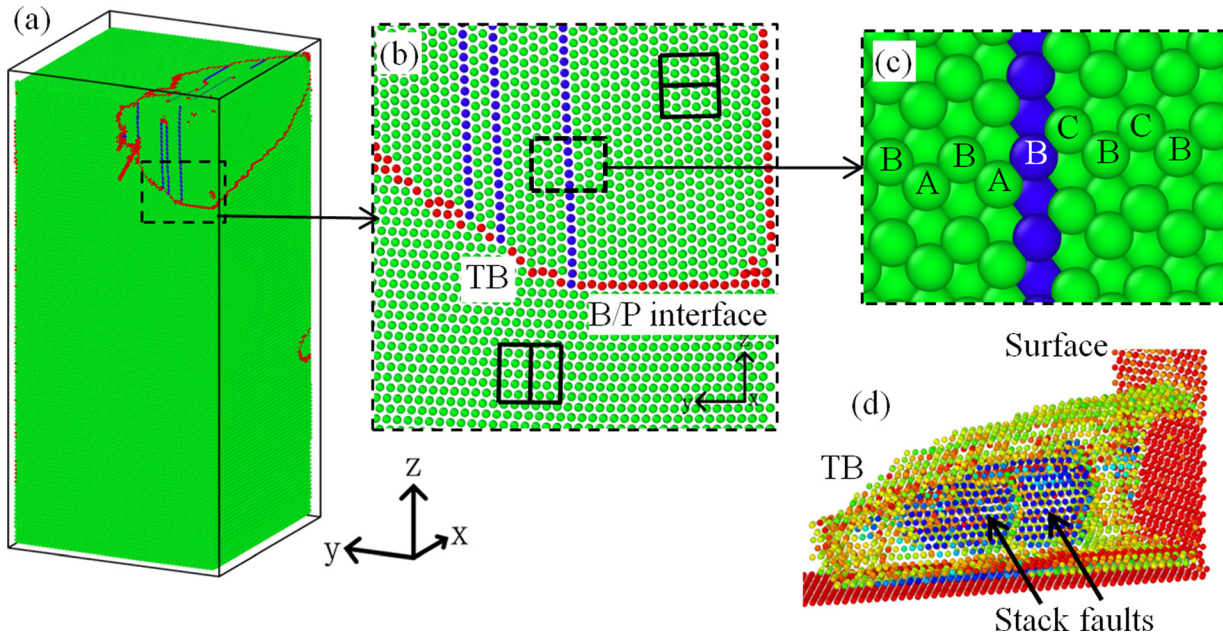


**Fig. 3** Uniaxial tension deformation for the  $\theta = 0$  deg case: (a) deformed cell at 5.48% strain (surface atoms are removed for visualization); (b) closeup view at the  $\{10-12\}$  TT boundary; (c) closeup view of the single layer stacking fault structure in the twin; and (d) nucleation of two stacking faults from the TB at 6.1% strain. All atoms are colored according to their CNA parameter in (a)–(c), where HCP atoms are green, FCC atoms are blue, and other atoms are red, and centrosymmetry parameter in (d) with HCP atoms removed (see online version for color).

observed that the nucleation stress decreases as the crystal  $c$ -axis deviates from the loading direction. In addition, twinning deformation dominates mostly the nucleation events, in particular:  $\{10-12\}$  tension twinning for  $\theta = 0$  deg;  $\{11-21\}$  tension twinning for  $\theta = 15-45$  deg; and  $\{10-11\}$  compression twinning for  $\theta = 60-90$  deg. A transition from tension twinning to compression twinning is expected to happen between orientations  $\theta = 45$  deg and 60 deg. To identify this transition angle, a simulation with an orientation angle of  $\theta = 55$  deg was conducted, which is also shown in Fig. 8. In this case, only basal dislocation slip is observed. This suggests that the transition angle from tension

twinning to compression twinning takes place close to  $\theta = 55$  deg. This transition angle can also be computed from three-dimensional strain analyses of the normal strain along  $c$ -axis, which can be expressed as

$$\varepsilon_c = -v\varepsilon_z \sin^2(\theta) + \varepsilon_z \cos^2(\theta) \quad (3)$$

Here, we assume the Mg crystals are isotropic with Poisson ratio  $v = 0.35$  for simplicity. Thus, Eq. (3) leads to a predicted transition angle of  $\theta = 59$  deg, which is in good agreement with current MD simulations.

In order to understand the orientation effects on the predicted deformation modes using Schmid factor analysis, the Schmid factor  $P(\theta)$  is calculated for each orientation angle. Then, the nucleation stress for any deformation mode can be calculated as

$$\sigma_N(q) = \tau_{CRSS}/P(\theta) \quad (4)$$

where  $\tau_{CRSS}$  is the critical resolved shear stress (CRSS) on the slip plane for dislocation-mediated plasticity, or the twinning plane for twinning mediated plasticity. Here, it is assumed that  $\tau_{CRSS}$  is constant for each deformation mode. Hence,  $\tau_{CRSS}$  can be computed by fitting the nucleation stress based on Eq. (4) with that predicted by the current MD simulations. For the present tension simulations,  $\tau_{CRSS}$  is shown to be: 1.5 GPa for TT<sub>1</sub>, 0.8 GPa for TT<sub>2</sub>, and 0.4 GPa for CT<sub>1</sub>. Finally, the Schmid factor analysis (i.e., Eq. (4)) is also shown in Fig. 8. It is observed that the three twinning deformation modes exhibit strong dependence on the Schmid factor, which also agrees well with the current MD results.

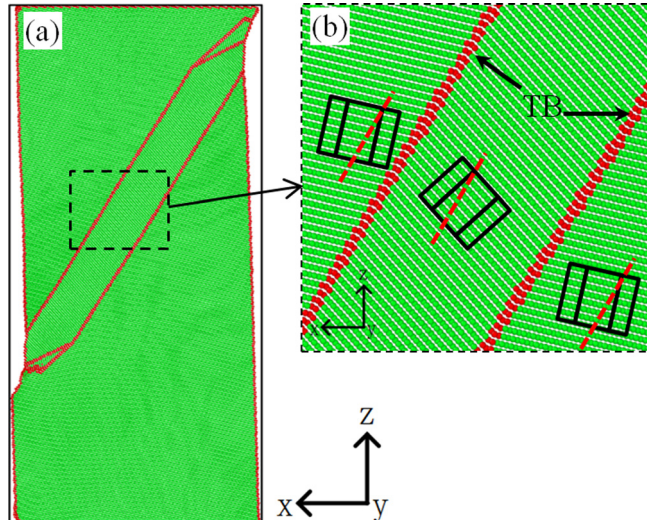


**Fig. 4** (a) Cross section through the  $\theta = 15$  deg simulation cell deformed to 4.68% strain in uniaxial tension using the Liu et al.'s potential and (b) closeup view of the  $\{11-21\}$  TT. All atoms are colored according to their CNA parameter, where HCP atoms are green, FCC atoms are blue, and other atoms are red (see online version for color).

**3.2 Uniaxial Compression Deformation.** Figure 9 shows the simulation results of four nanocrystals having their  $c$ -axis oriented by  $\theta = 0$  deg, 15 deg, 30 deg, and 45 deg from the compression loading axis. It should be noted that the  $\theta = 0$  deg case is a  $c$ -axis compression orientation and has been extensively studied experimentally (e.g., Refs. [3] and [7]), and by MD simulations (e.g., Refs. [11] and [12]). As shown in Fig. 9(a), the deformation is

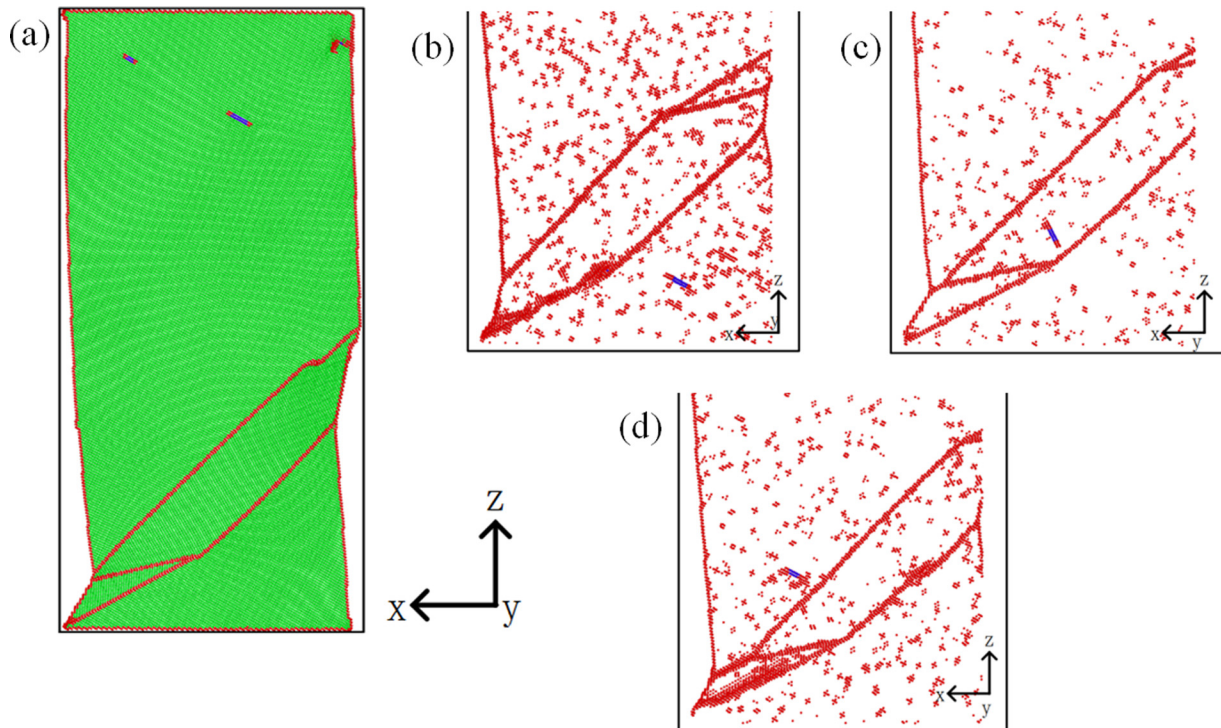


**Fig. 5** (a) Cross section through the  $\theta = 30$  deg simulation cell deformed to 5.08% strain in uniaxial tension. A sequence of snapshots showing an  $\langle a \rangle$  dislocation intersecting the  $\{11\bar{2}1\}$  TT is shown in (b) through (d). All atoms are colored according to their CNA parameter, where HCP atoms are green, FCC atoms are blue, and other atoms are red. In (b) through (d), all HCP atoms are removed to facilitate visualization (see online version for color).

mostly accommodated by  $\langle c+a \rangle$  dislocation slip, with hardly any twinning observed. The slip planes of these dislocations coincide with first-order pyramidal planes, in agreement with the previous studies [12,21]. It should be noted that in the study of Luque et al. [11], compression twinning rather than first-order pyramidal dislocations was observed in 10 nm nanocrystals. This is mainly a

result of the much smaller crystal sizes in that study, as compared to the first-order pyramidal slip in the 30 nm (current work) and 100 nm [12] crystals. This indicates the existence of a possible size-dependence on the deformation mode during  $c$ -axis compression. Consistent size-dependent deformation modes were also reported from micropillars (pyramidal slip [3–7]) and nanopillars

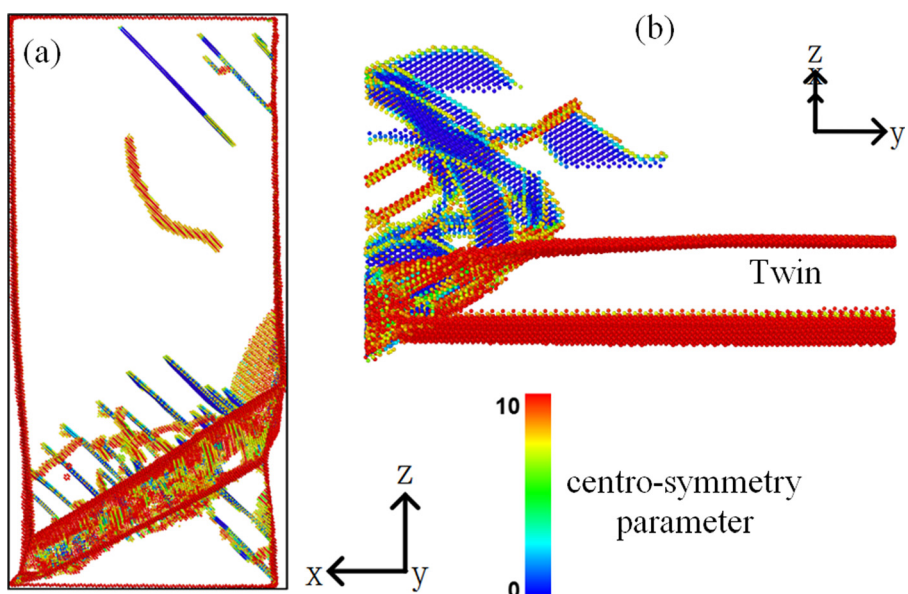


**Fig. 6** (a) Cross section through the  $\theta = 45$  deg simulation cell deformed to 5.08% strain in uniaxial tension. (b) Closeup view of the intersection of the  $\{11\bar{2}1\}$  TT with the free surface showing the nucleation of basal dislocations at the intersection. All atoms are colored by their centrosymmetry parameter, and HCP atoms are removed to facilitate visualization.

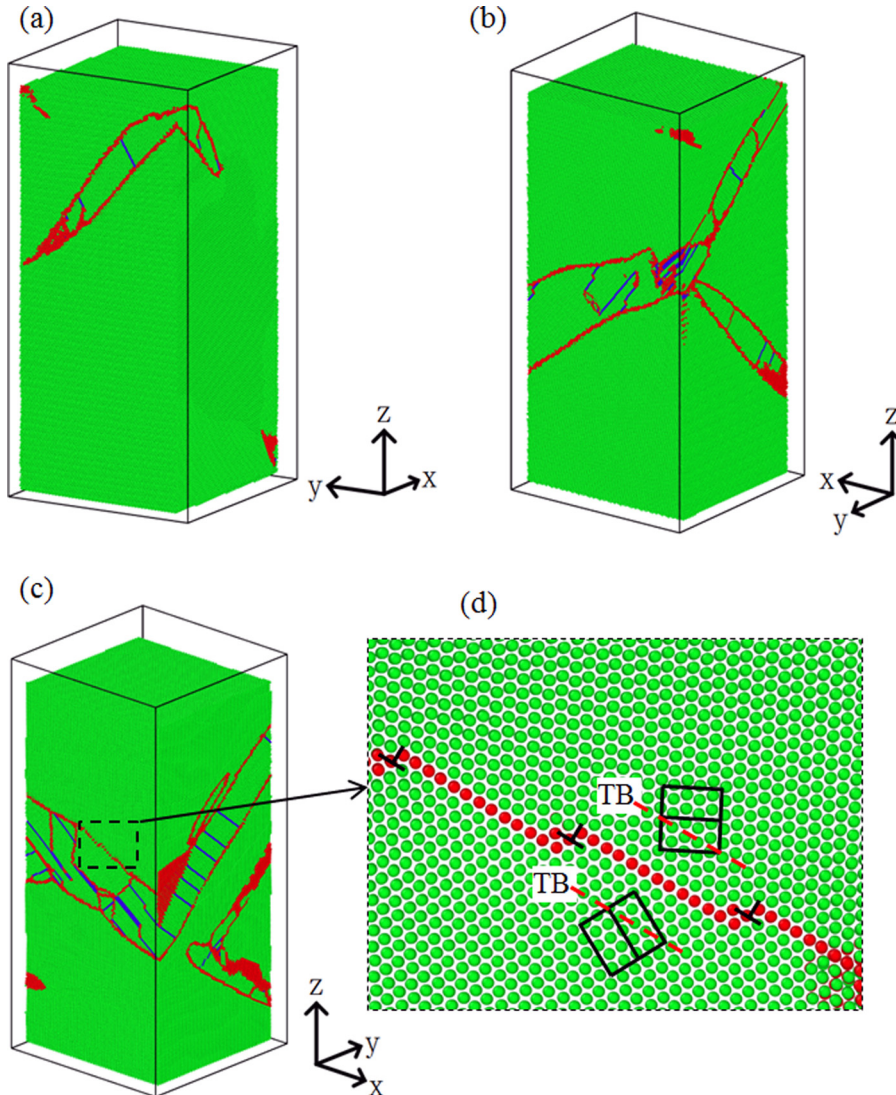


**Fig. 7** Uniaxial tension deformation of: (a)  $\theta = 60$  deg simulation cell at 4.28% strain; (b)  $\theta = 75$  deg simulation cell at 4.68% strain; and (c)  $\theta = 90$  deg simulation cell at 5.48% strain. (d) Closeup view of the  $\{10-11\}$  compression TB in (c). All atoms are colored according to their CNA parameter, where HCP atoms are green, FCC atoms are blue, and other atoms are red (see online version for color). Surface atoms are removed to facilitate visualization.

(compression twinning [8]) during  $c$ -axis compression experiments.

For the  $\theta = 15$  deg case, both first-order pyramidal  $\langle c+a \rangle$  dislocations, as well as basal dislocations play a dominant role, as shown in Fig. 9(b). With further deviation of the crystal  $c$ -axis from the compression loading axis, the Schmid factor on the basal plane increases, and basal slip becomes predominant at the orientation angle of  $\theta = 30$  deg (see Fig. 9(c)). Ultimately, at the orientation angle of  $\theta = 45$  deg, first-order pyramidal slip is completely suppressed (see Fig. 9(d)). These results are in good agreements with experimental observations for the same orientations [4,6,7,9,10].

The deformation details for the  $\theta = 60$  deg case are shown in Fig. 10. In addition to basal dislocations, a single large  $\{11-21\}$  tension twin is also observed. Based on Eq. (3), for this orientation, the  $c$ -axis strain is tensile in agreement with the observed tension twin system. Furthermore, Figs. 10(b) and 10(c) show a sequence of pre- and post-interactions between the  $\{11-21\}$  tension twin tip and a basal dislocation which was originally in the matrix. After the interaction, the intersected dislocation segment becomes a basal dislocation segment in the twin. Since twin

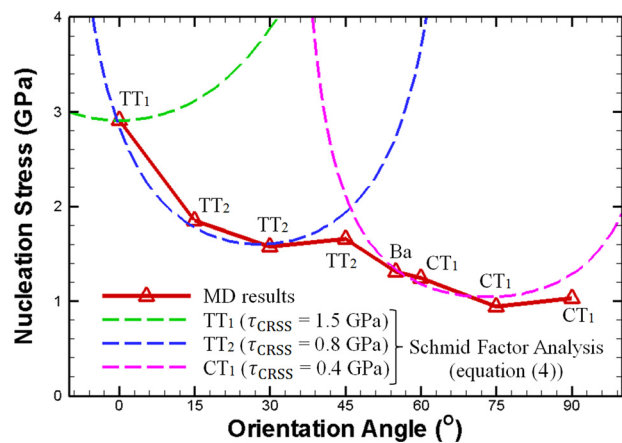


**Fig. 8** Nucleation stress and corresponding first deformation event as a function of the simulation cell orientation angle during uniaxial tension simulations. The following abbreviations are used: TT<sub>1</sub> for  $\{10-12\}$  TT; TT<sub>2</sub> for  $\{11-21\}$  TT; CT<sub>1</sub> for  $\{10-11\}$  CT; Ba for basal slip; Pr for prismatic slip; and Pyl for pyramidal I slip.

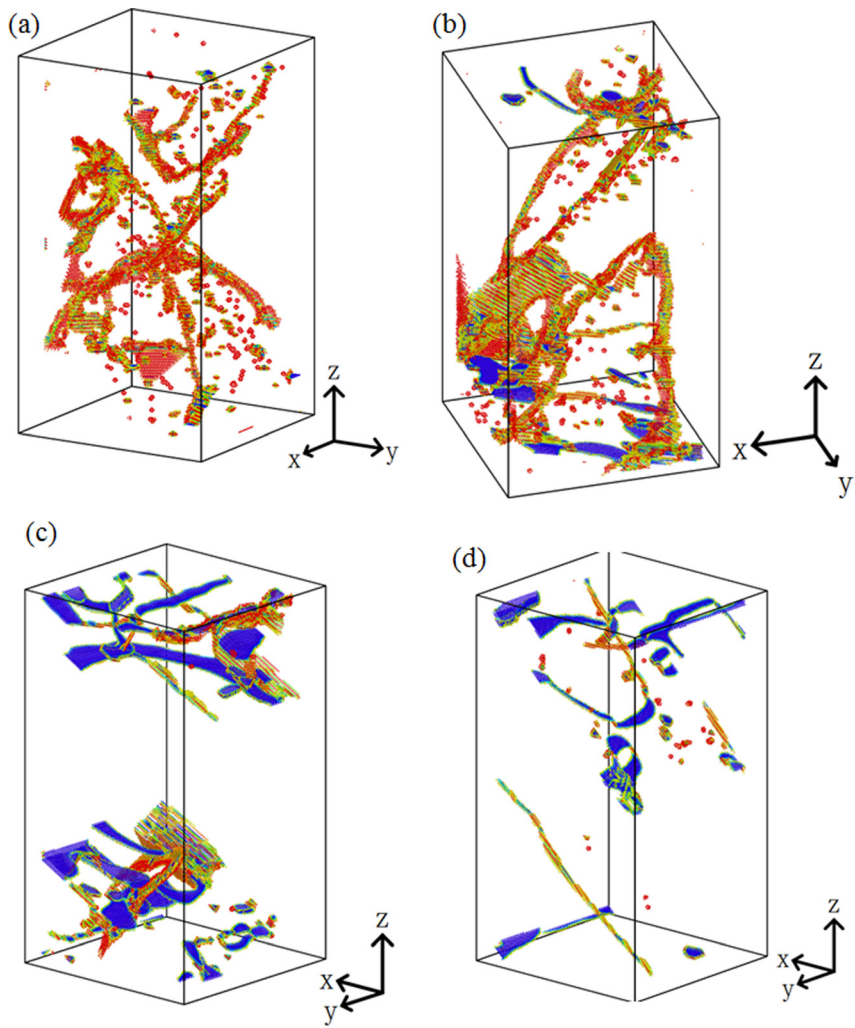


**Fig. 9** Uniaxial compression deformation for the: (a)  $\theta = 0$  deg case at 5.08% strain; (b)  $\theta = 15$  deg case at 5.08% strain; (c)  $\theta = 30$  deg case at 4.68% strain; and (d)  $\theta = 45$  deg case at 4.68% strain. All atoms are colored according to their centrosymmetry parameter. Surface and HCP atoms are removed to facilitate visualization.

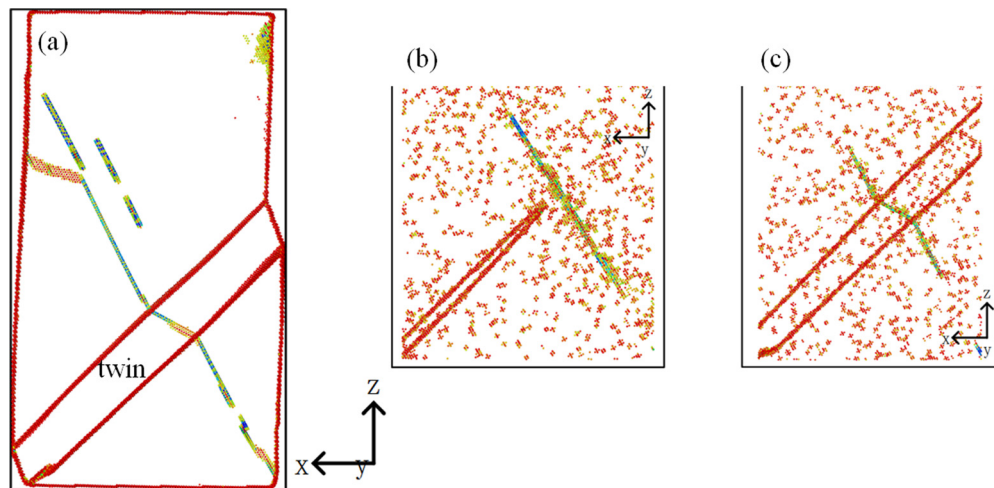


**Fig. 10** (a) Cross section through the  $\theta = 60$  deg simulation cell deformed to 4.68% strain in uniaxial compression. (b) Pre- and (c) post-snapshots of the interaction between a {11-21} TT and a basal dislocation. All the atoms are colored according to their centrosymmetry parameter. Surface and HCP atoms are removed to facilitate visualization.

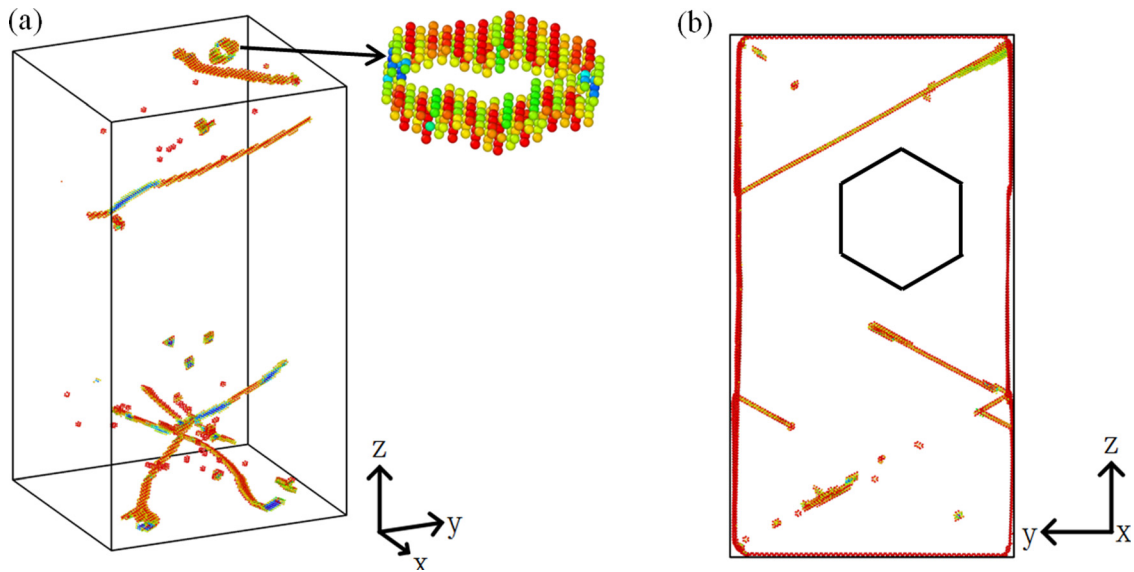
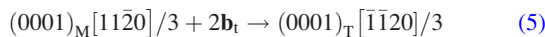
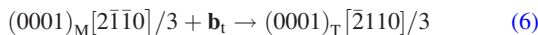


**Fig. 11** (a) Uniaxial compression deformation for the  $\theta = 75$  deg simulation cell at 5.08% strain. (b) Cross section through the  $\theta = 90$  deg simulation cell at 4.68% uniaxial compressive strain. Prismatic dislocations are apparent in both cases with the inset of (a) showing the formation of a dislocation loop. All the atoms are colored according to their centrosymmetry parameter. Surface and HCP atoms are removed to facilitate visualization.

growth is typically mediated by the glide of an array of twinning dislocations, this interaction process can be explained by the following reactions:



or



The remaining two compression simulations having  $\theta = 75$  deg and  $\theta = 90$  deg are shown in Fig. 11. Prismatic  $\langle a \rangle$  dislocations are observed to be predominant for both orientations. Many vacancies and interstitials are observed, which result from dislocation climb. In addition, multiple dislocation loops are also observed (see the inset of Fig. 11(a)), which also form as a result

of dislocation climb events. It should be noted that in the experiments of 90 deg orientated micropillars, TTs with boundaries on the  $\{10\bar{1}2\}$  plane (i.e.,  $TT_1$ ) were reported [4]. This discrepancy between micropillar experiments and MD simulations of nanopillars could be attributed to size-effects on deformation modes. In the Mg micropillars, the twinning deformation always exhibits a stronger size-effect on the yield stress than dislocation slip [4], i.e., the yield stress increases faster with the decreasing crystal diameter than the dislocation slip. This would lead to a critical diameter, below which dislocation slip dominates. Similar observations were reported for compression twinning in single-crystalline titanium alloy [32].

The nucleation stress and corresponding first deformation event during compression loading are shown in Fig. 12 as a function of simulation cell orientation angle. During compression loading, it is observed that the first deformation event is always dislocation slip, in particular: first-order pyramidal slip for  $\theta = 0$  deg, basal slip for  $\theta = 15\text{--}60$  deg, and prismatic slip for  $\theta = 75\text{--}90$  deg orientations. Furthermore, the nucleation stress decreases with increasing orientation angle up to  $\theta = 60$  deg, after which the nucleation stress subsequently increases. This is because basal slip is an easy slip mode as compared to first-order pyramidal and prismatic slips. Finally, by comparing the deformation modes and nucleation stresses during tension and compression loadings, a strong tension-compression asymmetry is clearly observed.

The Schmid factor analysis was also performed for the uniaxial compression loading, as shown in Fig. 12. In this case, it is seen that the deformation modes are weakly dependent on the Schmid factor.  $\tau_{CRSS}$  for PyI, Ba, and Pr slips is 0.8 GPa, 0.6 GPa, and 0.7 GPa, respectively. The nucleation stress for basal slip and pyramidal slip predicted by the Schmid factor analysis mostly agrees with the current MD simulations. However, the nucleation stress for prismatic slip is in strong disagreement. (For example, the Schmid factor for  $\theta = 90$  deg is larger than that at  $\theta = 75$  deg, but the nucleation stress as predicted by the current MD simulations is in fact higher for  $\theta = 90$  deg.)

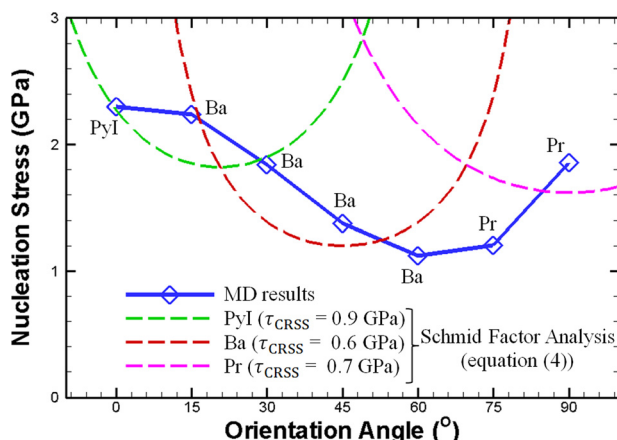


**Fig. 12** Nucleation stress and corresponding first deformation event as a function of the simulation cell orientation angle during uniaxial compression simulations. The following abbreviations are used: TT<sub>1</sub> for  $\{10\bar{1}2\}$  TT; TT<sub>2</sub> for  $\{11\bar{2}1\}$  TT; CT<sub>1</sub> for  $\{10\bar{1}1\}$  CT; Ba for basal slip; Pr for prismatic slip; and PyI for pyramidal I slip.

**3.3 Pure Bending Deformation.** The deformation modes during pure bending for different simulation cell orientation angles are shown in Fig. 13. For the  $\theta = 0$  deg case,  $\{10\bar{1}2\}$  tension twinning is dominant on the tension side, which agrees with

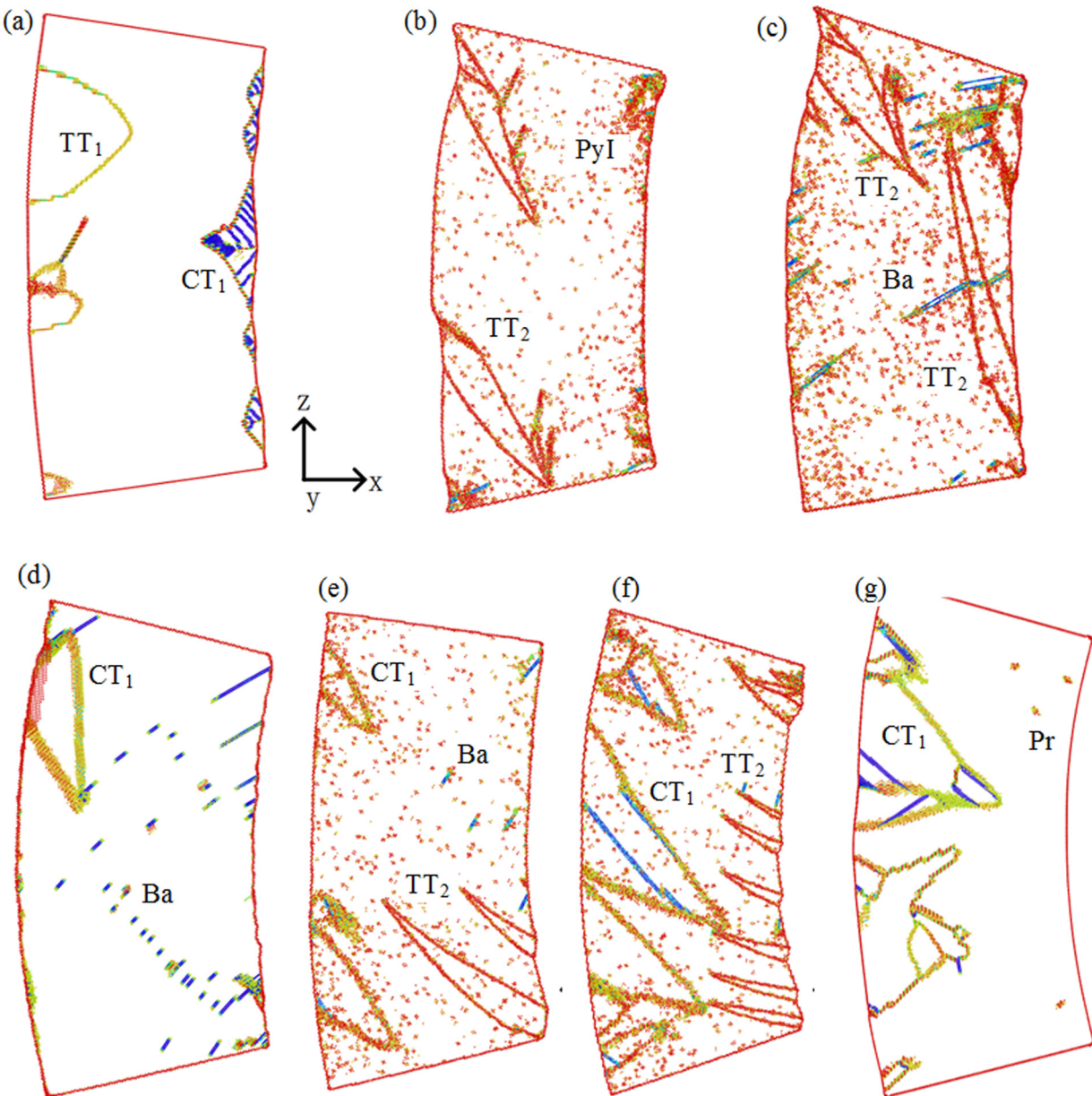


**Fig. 13** Cross sections showing the deformation modes during pure bending simulations for the: (a)  $\theta = 0$  deg case at a bending angle of 17.7 deg; (b)  $\theta = 15$  deg case at a bending angle of 16.8 deg; (c)  $\theta = 30$  deg case at a bending angle of 37.4 deg; (d)  $\theta = 45$  deg case at a bending angle of 28.4 deg; (e)  $\theta = 60$  deg case at a bending angle of 16.2 deg; (f)  $\theta = 75$  deg case at a bending angle of 32.5 deg; and (g)  $\theta = 90$  deg case at a bending angle of 31.7 deg. All the atoms are colored according to their centrosymmetry parameter. HCP atoms are removed to facilitate visualization.

the  $\theta=0$  deg case under uniaxial tension. On the other hand, {10–11} compression twinning is predominant on the compression side, which is not observed in the  $\theta=0$  deg case under uniaxial compression. It should be noted that inside the CTs, many intrinsic stacking faults are observed on basal planes. These are not basal dislocation stacking faults as suggested by Luque et al. [11] since they are single-atom-layer faults, as shown in Fig. 3. In the  $\theta=15$  deg case, {11–21} tension twinning is observed on the tension side, in agreement with the  $\theta=15$  deg case under uniaxial tension. On the compression side, pyramidal slip is mainly observed. For the  $\theta=30$  deg case, both {11–21} tension twinning and basal slip are observed on both the compression and tension sides. While the tension side agrees with the  $\theta=30$  deg case under uniaxial tension, the presence of the tension twinning on the compression side remains surprising.

In the  $\theta=45$  deg case, the tension and compression sides are dominated by {10–11} compressive twinning, and basal slip, respectively. These dislocations are clearly geometrically necessary dislocations [33]. The transition orientation angle from tension twinning activity to compression twinning activity on the tension side is clearly smaller than that during uniaxial tension loading.

For the  $\theta=60$  deg and 75 deg cases, on the tension and compression sides, {10–11} compression twinning and {11–21} tension twinning are observed, respectively. However, they are difficult to cross the neutral plane and interact with each other due to the bending constraint. These twins are also geometrically necessary twins [34]. Finally, for the  $\theta=90$  deg case, more compression twinning variants are observed on the tension side, while prismatic dislocations replace the TTs on the compression side, which

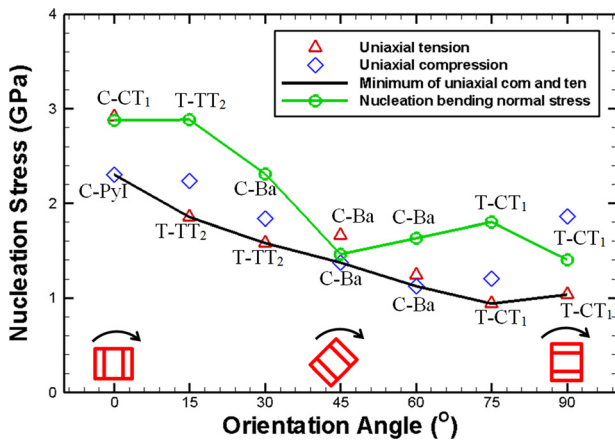


**Fig. 14 Nucleation stress and corresponding first deformation event as a function of the simulation cell orientation angle during pure bending simulations, as well as uniaxial tension and uniaxial compression. The following abbreviations are used: T- for tension side; C- for compression side; TT<sub>1</sub> for {10-12} TT; TT<sub>2</sub> for {11-21} TT; CT<sub>1</sub> for {10-11} CT; Ba for basal slip; Pr for prismatic slip; and Pyl for pyramidal I slip.**

agrees with the  $\theta = 90$  deg case under uniaxial tension and uniaxial compression, respectively. These predictions are also in good agreement with the cantilever nanobeam experiments of Yu et al. [8] showing compression twinning for this orientation.

In the current pure bending simulations, only a normal bending stress develops in the cross section. This normal stress is largest away from the neutral plane, as shown schematically in Fig. 2. Therefore, the maximum normal bending stress at the outermost edge controls the nucleation of the first deformation event. As a result, here we estimate the nucleation bending normal stress as

$$\sigma_N = \frac{M_N l_x}{2I_x} \quad (7)$$

where  $M_N$  is the nucleation moment and  $I_x$  is the area moment of inertia. This estimated nucleation bending normal stress is shown in Fig. 14 by the upper curve. The nucleation stresses for the uniaxial tension and uniaxial compression loadings are also shown in Fig. 14 as a function of the simulation cell orientation angle. The first nucleation deformation event and the corresponding side it occurs at are also indicated along the upper curve. The nucleation bending normal stress largely decreases with the increasing orientation angle, in agreement with uniaxial tension and uniaxial compression loading simulations. Since in bending simulations, the tension stress on the tension side is equal in magnitude to the compression stress on the compression side, the first nucleation event would be controlled by the weakest deformation mode on either side. The lower line in Fig. 14 denotes the lowest nucleation stress and weakest deformation mode of the uniaxial tension and compression simulations. It is clear that the first nucleating deformation mode during bending generally agrees with the weakest deformation mode during uniaxial loading. However, it should be noted that the nucleation stress in the bending simulations (upper curve) is always higher than the minimum nucleation stress of the uniaxial loading cases (lower curve), since the bending loading rate is higher.

## 4 Conclusions

Tension, compression, and bending deformations of single-crystalline magnesium nanocrystals were investigated using MD simulations. In particular, the crystal orientation effects were studied by increasing the *c*-axis orientation angle relative to the

loading direction. For tension loading, with increasing orientation angle, the deformation mode at yielding changes from tension twinning ( $\theta \leq 45$  deg) to compression twinning ( $\theta > 45$  deg). For compression loading, yielding is dominated by dislocation slips only, including first-order pyramidal slip for orientation angle  $\theta < 15$  deg, basal slip for orientation angle from  $\theta = 15$  deg to 60 deg, and prismatic slip for orientation angle  $\theta > 60$  deg. For bending simulations, yielding is mostly controlled by the weakest deformation mode between the compression and tension sides of the simulation cell. In general, the nucleation stress in each loading case largely decreases as the crystal *c*-axis deviates away from the loading direction. In addition to the MD simulations, Schmid factor analysis was also conducted to understand the orientation effects on the deformation modes.

## Acknowledgment

This research was sponsored by the Army Research Laboratory (#W911NF-12-2-0022). The views and conclusions contained in this document are those of the authors and should not be interpreted as representing the official policies, either expressed or implied, of ARL or U.S. Government. The U.S. Government is authorized to reproduce and distribute reprints for Government purposes notwithstanding any copyright notation herein. H.F. also gratefully acknowledges the financial support of Natural Science Foundation of China (11302140).

## References

- [1] Mises, R. V., 1928, "Mechanik der plastischen Formänderung von Kristallen," *J. Appl. Math. Mech.*, **8**(3), pp. 161–185.
- [2] Yoo, M. H., 1981, "Slip, Twinning, and Fracture in Hexagonal Close-Packed Metals," *Metall. Trans. A*, **12**(3), pp. 409–418.
- [3] Lilleodden, E., 2010, "Microcompression Study of Mg (0 0 0 1) Single Crystal," *Scr. Mater.*, **62**(8), pp. 532–535.
- [4] Kim, G. S., 2011, "Small Volume Investigation of Slip and Twinning in Magnesium Single Crystals," Ph.D. thesis, University of Grenoble, Grenoble, France.
- [5] Byer, C. M., Li, B., Cao, B., and Ramesh, K. T., 2010, "Microcompression of Single-Crystal Magnesium," *Scr. Mater.*, **62**(8), pp. 536–539.
- [6] Byer, C. M., and Ramesh, K. T., 2013, "Effects of the Initial Dislocation Density on Size Effects in Single-Crystal Magnesium," *Acta Mater.*, **61**(10), pp. 3808–3818.
- [7] Aitken, Z. H., Fan, H., El-Awady, J. A., and Greer, J. R., 2015, "The Effect of Size, Orientation and Alloying on the Deformation of AZ31 Nanopillars," *J. Mech. Phys. Solids*, **76**, pp. 208–223.
- [8] Yu, Q., Qi, L., Chen, K., Mishra, R. K., Li, J., and Minor, A. M., 2012, "The Nanostructured Origin of Deformation Twinning," *Nano Lett.*, **12**(2), pp. 887–892.
- [9] Ye, J., Mishra, R. K., Sachdev, A. K., and Minor, A. M., 2011, "In Situ TEM Compression Testing of Mg and Mg–0.2 wt.% Ce Single Crystals," *Scr. Mater.*, **64**(3), pp. 292–295.
- [10] Prasad, K. E., Rajesh, K., and Ramamurty, U., 2014, "Micropillar and Macropillar Compression Responses of Magnesium Single Crystals Oriented for Single Slip or Extension Twinning," *Acta Mater.*, **65**, pp. 316–325.
- [11] Luque, A., Ghazisaeidi, M., and Curtin, W. A., 2013, "Deformation Modes in Magnesium (0 0 0 1) and (01-11) Single Crystals: Simulations Versus Experiments," *Modell. Simul. Mater. Sci. Eng.*, **21**(4), p. 045010.
- [12] Tang, Y., and El-Awady, J. A., 2014, "Formation and Slip of Pyramidal Dislocations in Hexagonal Close-Packed Magnesium Single Crystals," *Acta Mater.*, **71**, pp. 319–332.
- [13] Guo, Y.-F., Xu, S., Tang, X.-Z., Wang, Y.-S., and Yip, S., 2014, "Twinability of HCP Metals at the Nanoscale," *J. Appl. Phys.*, **115**(22), p. 224902.
- [14] Fan, H., Aubry, S., Arsenlis, A., and El-Awady, J. A., 2015, "The Role of Twining Deformation on the Hardening Response of Polycrystalline Magnesium From Discrete Dislocation Dynamics Simulations," *Acta Mater.*, **92**, pp. 126–139.
- [15] Fan, H., Aubry, S., Arsenlis, A., and El-Awady, J. A., 2015, "Orientation Influence on Grain Size Effects in Ultrafine-Grained Magnesium," *Scr. Mater.*, **97**, pp. 25–28.
- [16] Fan, H., Aubry, S., Arsenlis, A., and El-Awady, J. A., 2015, "Discrete Dislocation Dynamics Simulations of Twin Size-Effects in Magnesium," *MRS Proc.*, **1741**, p. mrsf14-1741-aa1702-1702.
- [17] Fan, H., Aubry, S., Arsenlis, A., and El-Awady, J. A., 2015, "Grain Size Effects on Dislocation and Twinning Mediated Plasticity in Magnesium," *Scr. Mater.* (submitted).
- [18] Obara, T., Yoshinga, H., and Morozumi, S., 1973, "[11-22]-[1-123] Slip System in Magnesium," *Acta Metall.*, **21**(7), pp. 845–853.
- [19] Stohr, J.-F., Régnier, P., and Dupouy, J.-M., 1971, "Glissement non basal dans le magnésium," *Mém. Sci. Rev. Metall.*, **68**(1), pp. 49–54.

- [20] Fan, H., Hussein, A. M., and El-Awady, J., 2015, "Multiscale Modeling of the Size Effects on Plasticity in Metals," *Multiscale Mater. Modell. Nanomech.* (submitted).
- [21] Fan, H., and El-Awady, J. A., 2015, "Towards Resolving the Anonymity of Pyramidal Slip in Magnesium," *Mater. Sci. Eng. A* (submitted).
- [22] Xie, Y. X., and Hemker, K. J., 2015, personal communication.
- [23] Plimpton, S., 1995, "Fast Parallel Algorithms for Short-Range Molecular Dynamics," *J. Comput. Phys.*, **117**(1), pp. 1–19.
- [24] Sun, D. Y., Mendelev, M. I., Becker, C. A., Kudin, K., Haxhimali, T., Asta, M., Hoyt, J. J., Karma, A., and Srolovitz, D. J., 2006, "Crystal-Melt Interfacial Free Energies in HCP Metals: A Molecular Dynamics Study of Mg," *Phys. Rev. B*, **73**(2), p. 024116.
- [25] Liu, X.-Y., Adams, J. B., Ercolessi, F., and Moriarty, J. A., 1996, "EAM Potential for Magnesium From Quantum Mechanical Forces," *Modell. Simul. Mater. Sci. Eng.*, **4**(3), pp. 293–303.
- [26] Stukowski, A., 2010, "Visualization and Analysis of Atomistic Simulation Data With OVITO—the Open Visualization Tool," *Modell. Simul. Mater. Sci. Eng.*, **18**(1), p. 015012.
- [27] Sun, Q., Zhang, X. Y., Ren, Y., Tu, J., and Liu, Q., 2014, "Interfacial Structure of {10-12} Twin Tip in Deformed Magnesium Alloy," *Scr. Mater.*, **90-91**, pp. 41–44.
- [28] Barrett, C. D., El Kadiri, H., and Tschoop, M. A., 2012, "Breakdown of the Schmid Law in Homogeneous and Heterogeneous Nucleation Events of Slip and Twinning in Magnesium," *J. Mech. Phys. Solids*, **60**(12), pp. 2084–2099.
- [29] Aghababaei, R., and Joshi, S. P., 2014, "Micromechanics of Tensile Twinning in Magnesium Gleaned From Molecular Dynamics Simulations," *Acta Mater.*, **69**, pp. 326–342.
- [30] Stanford, N., 2008, "Observation of {1121} Twinning in a Mg-Based Alloy," *Philos. Mag. Lett.*, **88**(5), pp. 379–386.
- [31] Yoo, M. H., 1969, "Interaction of Slip Dislocations With Twins in HCP Metals," *Trans. Metall. Soc. AIME*, **245**, pp. 1841–2114.
- [32] Yu, Q., Shan, Z.-W., Li, J., Huang, X., Xiao, L., Sun, J., and Ma, E., 2010, "Strong Crystal Size Effect on Deformation Twinning," *Nature*, **463**(7279), pp. 335–338.
- [33] Gao, H., and Huang, Y., 2003, "Geometrically Necessary Dislocation and Size-Dependent Plasticity," *Scr. Mater.*, **48**(2), pp. 113–118.
- [34] Gil Sevillano, J., 2008, "Geometrically Necessary Twins and Their Associated Size Effects," *Scr. Mater.*, **59**(2), pp. 135–138.